Energy Engineering

Tech Science Press

Doi:10.32604/ee.2026.072845

ARTICLE

Hierarchical Coordinated Optimization Control Strategy for Electricity-Hydrogen DC Microgrid System

Xinhao Lin[1], Lei Yu[1], Shuyin Duan[1], Yinliang Liu[1], Lvzerui Yuan[1], Xiao Chen[1,*] and Yiqing Lian[2]

[1]Department of Power Distribution Technology, Electric Power Research Institute of China Southern Power Grid Corporation, Guangzhou, 510663, China

[2]Department of Technological Innovation, China Southern Power Grid, Guangzhou, 510663, China

*Corresponding Author: Xiao Chen. Email: xiaochen8392025@163.com

Received: 04 September 2025; Accepted: 03 December 2025; Published: 27 May 2026

ABSTRACT: To address the operational challenges posed by renewable energy generation uncertainty and load fluctuations in DC microgrids, this paper proposes a hierarchical coordinated optimization control strategy for electricity-hydrogen hybrid DC microgrids (EH-DC-MG). The strategy aims to leverage the synergistic advantages of hybrid electricity-hydrogen energy storage to simultaneously achieve multiple objectives, including economic system operation, efficient utilization of renewable energy, and reliable power supply. The upper optimization scheduling layer formulates a mixed-integer linear programming model with the objective of minimizing the total system cost, which incorporates equipment operation and maintenance expenses, battery depreciation, penalties for renewable energy curtailment, and power/hydrogen supply shortages. By solving this model, optimal power reference signals are generated for devices. The lower device control layer employs designed DC/DC converter control strategies to ensure fast and accurate tracking of the optimization commands while maintaining DC bus voltage stability. Simulation results demonstrate that the proposed strategy can effectively coordinate electricity-hydrogen energy conversion and storage. Under various typical and extreme scenarios, the system maintains a high renewable energy utilization rate—remaining above 97.572% even under extreme conditions—while keeping the power shortage rate and hydrogen load curtailment rate at low levels. Specifically, under extreme power deficit scenarios, these rates are limited to 2.003% and 5.081%, respectively, which are significantly below the 10% quality constraint threshold, thereby ensuring a high degree of supply reliability. In addition, the DC bus voltage fluctuation is stabilized within 0.37%, far below the 5% safety operation threshold, validating the effectiveness of the control strategy. This study confirms that the proposed hierarchical coordinated optimization control strategy can support electricity-hydrogen hybrid DC microgrids in achieving economical, reliable, and resilient operation, providing a key technical reference for the optimized management of microgrids with high penetration of renewable energy.

KEYWORDS: Electric-hydrogen; DC microgrid; coordinated optimization; control strategy

1 Introduction

The global energy landscape has witnessed widespread adoption of renewable energy sources such as wind and solar power, driven by escalating fossil fuel depletion and environmental degradation concerns [1,2]. The power generation of renewable energy is highly susceptible to multiple complex factors such as meteorological conditions and geographical environments, exhibiting strong uncertainty [3]. Consequently, the large-scale integration of renewable energy poses significant challenges to power systems.

Copyright © 2026 The Authors. Published by Tech Science Press.
This work is licensed under a Creative Commons Attribution 4.0 International License, which permits unrestricted use, distribution, and reproduction in any medium, provided the original work is properly cited.

Hydrogen energy is hailed as the "ultimate energy source" of the 21st century due to its extensive storage capacities and long storage cycles [4]. Utilizing renewable energy for water electrolysis to produce hydrogen transforms the strongly intermittent nature of renewable sources into storable hydrogen energy, effectively mitigating the high volatility of renewable power generation [5]. Relying on energy storage and conversion devices such as battery energy storage (BES), Hydrogen Storage Tank (HST), electrolyzer (EZ), and fuel cell (FC) to achieve coordinated operation and integrated development of electricity-hydrogen energy is a critical pathway for realizing long-term, large-scale electricity storage [6]. However, various electric-hydrogen resources exhibit significantly different operating characteristics, thus integrating multiple electric-hydrogen resources into distribution networks and achieving their efficient coordinated operation still poses numerous technical challenges. For example, BES exhibits rapid response capabilities but low energy density [7], while EZ and FC demonstrate significant differences in start-stop characteristics and operational efficiency [8]. Coordinating various electric-hydrogen resources across different time scales and operating conditions to optimize energy flow and conversion efficiency has become key to enhancing the flexibility and stability of power systems. Additionally, the coupling operation of electricity-hydrogen systems involves complex safety constraints, economic dispatch, and control strategies, urgently requiring the development of refined collaborative operation models and intelligent regulation methods to support efficient integration and stable power supply for power systems with high-penetration renewable energy [9].

DC microgrids facilitate the deep integration of distributed renewable energy sources, effectively mitigating the imbalance between energy supply and demand [10]. Energy storage technology plays a critical role in microgrid systems, ensuring their stability and reliability through its peak shaving and valley filling functions [11]. Compared to traditional battery energy storage systems, integrated electricity-hydrogen energy storage is more suitable for long-term and large-scale energy storage needs, significantly enhancing energy utilization efficiency [12]. However, the typical architecture and operational modes of integrated electricity-hydrogen energy systems remain inadequately defined, and the coordinated dispatch of electrical energy storage, hydrogen energy storage, and power-to-hydrogen conversion equipment requires further investigation.

Currently, research on control strategies for electric-hydrogen coupled DC microgrid systems primarily focuses on energy management and stability maintenance aspects. Existing control strategies can be primarily categorized into the following classes: rule-based control strategies [13–15], model predictive control strategies [16,17], and optimization algorithm-driven intelligent control strategies [18–22]. However, most existing control strategies focus on short-term energy balance, voltage stabilization, or operational cost minimization, lacking effective optimization for long-term economic optimality.

The validation of microgrid operation strategies is predominantly based on a limited number of typical daily scenarios, aiming to demonstrate the basic functionality and economic performance of control strategies under normal operating conditions. For instance, ref. [16] employed a distributed economic model predictive control (DEMPC) approach to manage a PV/hydrogen DC microgrid, with a primary focus on optimizing daily operational costs; ref. [19] utilized an intelligent agent-based method for energy management in an islanded AC/DC hybrid microgrid, enhancing system adaptability under typical conditions; ref. [22] applied a data-driven deep reinforcement learning technique to optimize the peak-to-average ratio and profit in a multi-microgrid system. However, the assessment of strategy robustness under extreme conditions, such as prolonged insufficient renewable generation or severe power surplus, is often absent. This lack of stress testing fails to provide convincing evidence for the practical application and reliability of the strategies in real-world environments where extreme events are inevitable.

This paper proposes a hierarchical coordinated optimal control method for EH-DC-MG, which fully considers the coordinated operation of electricity and hydrogen as well as the differences among various

devices, aiming to achieve economical operation, renewable energy accommodation, energy supply and coordinated control of the EH-DC-MG. The contributions of this paper are threefold:

1) A typical architecture for an EH-DC-MG is developed. This framework innovatively integrates the hydrogen energy system comprising the EZ, HST and FC with the BES, leveraging hydrogen's suitability for long-term, large-scale energy storage and batteries' capability for rapid response to form a complementary hybrid energy storage system. This work provides an important reference for developing optimal scheduling models and operational simulations. A hierarchical coordinated optimal control strategy for EH-DC-MG based on MILP is proposed, aiming to determine the optimal operating states of equipment to minimize system costs. By adopting appropriate control methods for DC/DC converters, the tracking of optimal dispatch commands is achieved while ensuring stable system operation.

2) A hierarchical coordinated optimal control strategy for EH-DC-MG is proposed, which decomposes the complex system management problem into an "optimization dispatch layer" and a "device control layer". The upper layer employs a mixed-integer linear programming (MILP) model with the objective of minimizing the total system cost (including operation and maintenance, penalty costs for energy curtailment and power shortage, and battery depreciation) to generate a globally optimal day-ahead dispatch schedule. The lower layer designs corresponding local control strategies to achieve precise power tracking for the devices by controlling the DC/DC converters, where the battery adopts constant voltage control to maintain the bus voltage stability.

3) To thoroughly validate the effectiveness of the proposed strategy, this study analyzes not only 23 typical daily scenarios but also tests two extreme scenarios characterized by severe scarcity and extreme abundance of renewable resources. The results demonstrate that even under these extreme conditions, the strategy maintains the State of Energy (SOE) of the HST and the State of Charge (SOC) of the BES within safe operating ranges, while achieving high renewable energy utilization rates and extremely low energy shortage rates. This provides critical quantitative basis and practical guidance for the engineering application of electricity-hydrogen hybrid energy storage systems in real-world complex environments.

2 Modelling of the EH-DC-MG

2.1 The Typical Form of EH-DC-MG

Fig. 1 shows the typical form of EH-DC-MG.

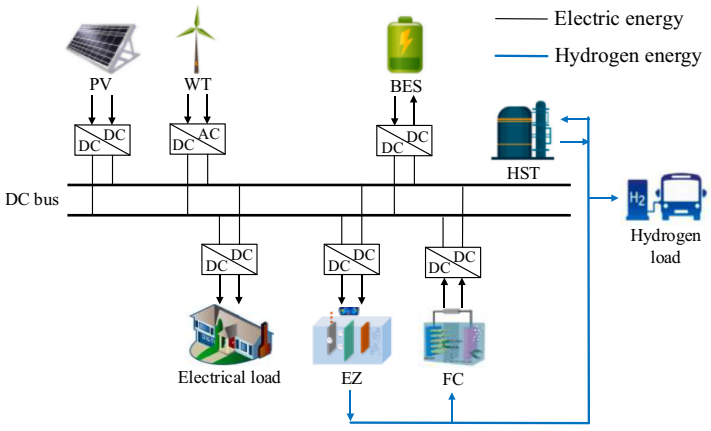

Figure 1: Overview of an EH-DC-MG

The system's power generation is provided by PV arrays and wind turbines (WTs). The PV arrays are connected to the DC bus through unidirectional DC/DC converters, typically operating in Maximum Power Point Tracking (MPPT) mode, while the WTs are interfaced with the DC bus via unidirectional AC/DC converters, also generally employing MPPT control strategy. The system incorporates two types of energy storage devices: hydrogen storage tank (HST) and battery bank. The BES is connected through bidirectional DC/DC converters, with its charging and discharging operations regulating the DC bus power balance. The hydrogen storage system consists of HST, coupled with power-to-hydrogen conversion equipment including EZs and FCs. The EZs produce hydrogen through water electrolysis, facilitating electricity-to-hydrogen energy conversion, and are connected via unidirectional DC/DC converters. Conversely, the FCs generate electricity through hydrogen electrochemical conversion (hydrogen-to-power) and are similarly interfaced using unidirectional DC/DC converters. All electrical loads in this DC microgrid are inherently DC-compatible and are connected to the DC bus through unidirectional DC/DC converters, completing the system's integrated architecture for renewable energy utilization, multi-form energy storage, and efficient power distribution. Additionally, the system incorporates a dedicated hydrogen energy pathway. The hydrogen produced by the EZs is stored in the HST. When the microgrid is short of power or there is a demand from the hydrogen load, the HST releases hydrogen to simultaneously supply the FCs for power generation and meet the hydrogen load demand.

2.2 Electricity and Hydrogen Storage and Conversion Model

2.2.1 Hydrogen Storage Tank Model

The hydrogen storage rate of the HST is mathematically expressed by Eq. (1).

$$m_t^{\mathrm{HST}} = m_t^{\mathrm{in}} - m_t^{\mathrm{out}} - m_t^{\mathrm{leak}} \tag{1}$$

where m_t^{HST}, m_t^{in}, m_t^{out} and m_t^{leak} represent the hydrogen storage or discharge rate of the HST, the hydrogen flow rate input from the EZs to the tank, the hydrogen output rate from the tank and the hydrogen leakage rate from the tank, respectively.

Eq. (2) represents the net hydrogen input in terms of molar quantity for the hydrogen storage tank during the time period from 0 to t_0 when hydrogen leakage is neglected.

$$n_{\mathrm{t}}^{\mathrm{H}} = \int_0^{\mathrm{t}} m_t dt \tag{2}$$

where $n_{\mathrm{t}}^{\mathrm{H}}$ is the net hydrogen input of the HST; m_t is the hydrogen storage rate after ignoring hydrogen leakage.

Eq. (3) represents the state of energy (SOE) of the HST at time t based on the ideal gas equation of state.

$$SOE_{t_0} = \frac{\frac{\mathrm{R}T_{\mathrm{HST}}n_t^{\mathrm{H}}}{V_{\mathrm{ra}}^{\mathrm{HST}}} + U_0^{\mathrm{HST}}}{U_{\mathrm{ra}}^{\mathrm{HST}}} \tag{3}$$

where R is the molar gas constant; T_{HST} is the internal storage temperature of the HST; $V_{\mathrm{ra}}^{\mathrm{HST}}$ is the rated volumetric capacity of the HST; U_0^{HST} and $U_{\mathrm{ra}}^{\mathrm{HST}}$ are the initial pressure and rated pressure of the HST, respectively.

Eq. (4) represents the electrical power consumed by the compressor.

$$P_t^{\mathrm{CP}} = a^{\mathrm{CP}} m_t^{\mathrm{in}} \tag{4}$$

where P_t^{CP} is the power of the compressor at time t; a^{CP} is the power consumption coefficient of the compressor in hydrogen compression.

Eqs. (5) and (6) constrain the SOE of HST.

$$SOE_t = SOE_{t-1} + \frac{1}{m_{ra}^{HST}}\left(\eta^{HST,ch} m_t^{ch} - \frac{m_t^{dis}}{\eta^{HST,dis}}\right)\Delta t \tag{5}$$

$$SOE_{min} \le SOE_t \le SOE_{max} \tag{6}$$

where m_{ra}^{HST} is the rated storage mass of the HST; $\eta^{HST,ch}$ and $\eta^{HST,dis}$ are the hydrogen storage and output efficiency of the HST, respectively; m_t^{ch} and m_t^{dis} are the hydrogen storage and release rates of the HST at time t, respectively; Δt is the scheduling time interval; SOE_{min} and SOE_{max} are the lower and upper limits of SOE, respectively.

Eqs. (7) and (8) are constraints on the hydrogen charging and discharging rates of HST, and Eq. (9) restricts HST from simultaneously charging and discharging hydrogen.

$$0 \le m_t^{ch} \le B_t^{HST,ch} m_{max}^{HST} \tag{7}$$

$$0 \le m_t^{dis} \le B_t^{HST,dis} m_{max}^{HST} \tag{8}$$

$$0 \le B_t^{HST,ch} + B_t^{HST,dis} \le 1 \tag{9}$$

where $B_t^{HST,ch}$ and $B_t^{HST,dis}$ denote the binary variables indicating the charging and discharging states of HST at time t, respectively; m_{max}^{HST} is the maximum hydrogen charging and discharging rate of HST.

2.2.2 Battery Energy Storage Model

Eq. (10) represents the output voltage of lithium battery [23].

$$U_{bat} = E_0 - K_e\frac{Q}{Q-I}I + A_b \exp(-BI) - R_{res}I^* - R_b I_{bat} \tag{10}$$

where E_0 denotes the open-circuit voltage constant; K_e represents the polarization constant characterizing overpotential effects; Q indicates the maximum available capacity under standard testing conditions. I is available energy between cutoff voltages; I^* is the low-frequency dynamic current; A_b is exponential zone amplitude; B is the inverse time constant of exponential zone; R_{res} is the polarization resistance; I_{bat} is the battery charge/discharge current; R_b is the internal resistance of battery.

The state of charge (SOC) can be calculated using Eq. (11). Eqs. (12) and (13) are constraints on the SOC of BES.

$$SOC_t = \left[1 - \frac{1}{Q}\int_0^t I_{bat}(t)\,dt\right] \times 100\% \tag{11}$$

$$SOC_t = (1-\tau)\,SOC_{t-1} + \frac{1}{E_{ra}^{BES}}\left(P_t^{ch}\eta^{BES,ch} - \frac{P_t^{dis}}{\eta^{BES,dis}}\right)\Delta t \tag{12}$$

$$SOC_{min} \le SOC_t \le SOC_{max} \tag{13}$$

where τ, E_{ra}^{BES}, $\eta^{BES,ch}$ and $\eta^{BES,dis}$ respectively represent the self-discharge rate, rated capacity, charging efficiency and discharging efficiency of BES; SOC_t illustrates the SOC of BES at time t; SOC_{min} and SOC_{max} are the upper and lower limits of SOC, respectively; P_t^{dis} and P_t^{ch} represent the battery discharge power and charge power at time t, respectively.

Eqs. (14)–(17) constrain the range of charging and discharging power of BES, and Eq. (18) restricts that BES cannot charge and discharge simultaneously. The relationship between rated power and rated capacity is shown as Eq. (19).

$$0 \le P_t^{\mathrm{dis}} \le B_t^{\mathrm{BES,dis}} P_{\mathrm{ra}}^{\mathrm{BES}} \tag{14}$$

$$P_t^{\mathrm{dis}} \ge 0 \tag{15}$$

$$0 \le P_t^{\mathrm{ch}} \le B_t^{\mathrm{BES,ch}} P_{\mathrm{ra}}^{\mathrm{BES}} \tag{16}$$

$$P_t^{\mathrm{ch}} \ge 0 \tag{17}$$

$$0 \le B_t^{\mathrm{BES,dis}} + B_t^{\mathrm{BES,ch}} \le 1 \tag{18}$$

$$P_{\mathrm{ra}}^{\mathrm{BES}} = 0.5 E_{\mathrm{ra}}^{\mathrm{BES}} \tag{19}$$

where $P_{\mathrm{ra}}^{\mathrm{BES}}$ represents the rated power; $B_t^{\mathrm{BES,dis}}$ and $B_t^{\mathrm{BES,ch}}$ denote the binary variables indicating the discharging and charging states of BES at time t, respectively.

2.2.3 Fuel Cell Model

A FC is a device that converts chemical energy from fuel into electrical energy. The proton exchange membrane fuel cell (PEMFC) has been selected due to its high efficiency, rapid response characteristics, and excellent modular adaptability. According to [24], the empirical expression for the output voltage of a single FC unit can be represented as Eq. (20). The output voltage of the FC stack is expressed by Eq. (21).

$$U_{\mathrm{cell}}^{\mathrm{FC}} = E_{\mathrm{ner}} - U_{\mathrm{act}} + U_{\mathrm{ohm}} + U_{\mathrm{con}} \tag{20}$$

$$U^{\mathrm{FC}} = n^{\mathrm{FC}} U_{\mathrm{cell}}^{\mathrm{FC}} \tag{21}$$

where $U_{\mathrm{cell}}^{\mathrm{FC}}$ is the output voltage of the FC unit; E_{ner} represents the nernst potential of the PEMFC; U_{act}, U_{ohm}, and U_{con} denote the activation overpotential, ohmic overpotential, and concentration overpotential, respectively, which collectively characterize the polarization losses in the PEMFC. U^{FC} represents the FC stack output voltage, and n^{FC} is the number of FC unites.

Eqs. (22) and (23) represent the hydrogen consumption rate and oxygen consumption rate respectively during FC operation.

$$v_{\mathrm{fuel}}^{\mathrm{FC}} = \frac{60000 \mathrm{R} T_{\mathrm{FC}} n^{\mathrm{FC}} i^{\mathrm{FC}}}{z \mathrm{F} P_{\mathrm{fuel}} U_{\mathrm{H}} x\%} \tag{22}$$

$$v_{\mathrm{air}}^{\mathrm{FC}} = \frac{60000 \mathrm{R} T_{\mathrm{FC}} n^{\mathrm{FC}} i^{\mathrm{FC}}}{z \mathrm{F} P_{\mathrm{air}} U_{\mathrm{O}} y\%} \tag{23}$$

where $v_{\mathrm{fuel}}^{\mathrm{FC}}$ and $v_{\mathrm{air}}^{\mathrm{FC}}$ represent the volumetric flow rates of hydrogen and air, respectively; i^{FC} is the FC stack current; z represents transferred electrons per reaction; F is the Faraday constant; U_{H} and U_{O} represent the utilization of hydrogen and oxygen, respectively; x and y are the volumetric concentration percentages of hydrogen and oxygen, respectively; P_{fuel} and P_{air} are the pressures of hydrogen and oxygen, respectively; T_{FC} is the operating temperature of the FC.

The linearized expression for the relationship between the power consumption of the fuel cell and the hydrogen production rate is shown as Eq. (24).

$$m_t^{\mathrm{FC}} = \frac{P_t^{\mathrm{FC}}}{\eta^{\mathrm{FC}} \mathrm{H}} \tag{24}$$

where m_t^{FC} and P_t^{FC} represent the hydrogen consumption rate and the power generation output of the FC at time t; η^{FC} indicates the energy conversion efficiency of the FC, and H stands for the heating value of hydrogen.

η^{FC} varies with the load rate of the FC. The segmented values of η^{FC} and the load rate of the FC are given by Eqs. (25) and (26), respectively.

$$\eta_t^{FC} = \begin{cases} \eta_{low}^{FC}, 0 < W^{FC} \le 20\% \\ \eta_{mid1}^{FC}, 20\% < W^{FC} \le 50\% \\ \eta_{mid2}^{FC}, 50\% < W^{FC} \le 90\% \\ \eta_{high}^{FC}, 90\% < W^{FC} \le 100\% \end{cases} \tag{25}$$

$$W^{FC} = \frac{P_t^{FC}}{P_{rate}^{FC}} \tag{26}$$

where W^{FC} represents the load rate of the FC; η_{low}^{FC}, η_{mid1}^{FC}, η_{mid2}^{FC}, and η_{high}^{FC} denote the electro-hydrogen conversion efficiencies of the FC under different load rate segments.

2.2.4 Electrolyzer Model

The EZ can be equivalently modeled as a nonlinear DC load, and the voltage-current (U-I) characteristic expression for a single EZ is shown as Eq. (27), and Eq. (28) represents the output voltage of the EZ stack [25].

$$U_{cell}^{EZ} = U_r + \frac{r_1 + r_2 T_{EZ}}{S} I^{EZ} + k^{EZ} \ln\left(\frac{k_1 + \frac{k_2}{T_{EZ}} + \frac{k_3}{T_{EZ}^2}}{S} I^{EZ} + 1 \right) \tag{27}$$

$$U^{EZ} = n^{EZ} U_{cell}^{EZ} \tag{28}$$

where U_{cell}^{EZ} and U^{EZ} represent the voltage of the EZ cell and the EZ stack, respectively; r_1 and r_2 denote the ohmic resistance parameters of the EZ, respectively; T_{EZ} indicates the operating temperature of the EZ; S stands for the surface area of the EZ electrodes; I^{EZ} is the operating current of the EZ; k^{EZ}, k_1, k_2, and k_3 are the overpotential parameters of the EZ; U_r represents the reversible voltage of the EZ; n^{EZ} represents the number of series-connected EZ cells.

The relationship between U_r and temperature is shown as Eq. (29).

$$U_r = U_r^0 - k_r \left(T_{EZ} - 298.15 \right) \tag{29}$$

where U_r^0 is the reversible voltage under standard conditions; k_r is the empirical temperature coefficient of the reversible voltage.

The relationship between the hydrogen production rate of the electrolyzer and the operating current at the corresponding time is shown in Eq. (30), and Eq. (31) represents the hydrogen production rate of the EZ stack.

$$q_{H,c} = \frac{\eta_F I^{EZ}}{2F} \tag{30}$$

$$q_H = n^{EZ} q_{H,c} \tag{31}$$

where $q_{H,c}$ is the hydrogen production rate of the electrolysis unit; η_F is the current efficiency of the EZ; q_H is the hydrogen production rate of the EZ stack.

The empirical formula for η_F is shown as Eq. (32).

$$\eta_F = \frac{\left(I^{EZ}/S\right)^2}{k_{f1} + \left(I^{EZ}/S\right)^2} k_{f2} \tag{32}$$

where k_{f1} and k_{f2} represent the current efficiency parameters of the EZ.

During optimization modeling, the relationship between hydrogen production rate and EZ stack power consumption is linearly approximated, as shown in Eq. (33).

$$m_t^{EZ} = \frac{\eta^{EZ} P_t^{EZ}}{H} \tag{33}$$

where m_t^{EZ} is the hydrogen production rate of the EZ stack at time t; η^{EZ} is the electrolysis efficiency of the EZ stack; P_t^{EZ} is the electrolysis power consumption of the EZ stack at time t.

3 Coordinated Optimization Control Strategy for EH-DC-MG

In this paper, the DC microgrid system operates in islanded mode and adopts a hierarchical coordinated energy management architecture consisting of an optimization layer and a control layer. The upper optimization layer performs long-term scheduling and planning. Using MILP, it coordinates the power allocation of the BES, HST, FC, and EZ in each time period based on renewable energy output, and load demand, the SOE of the HST and SOC of the BES. The objective is to achieve long-term economic optimization and improve renewable energy utilization.

3.1 Device Control Layer

The hierarchical coordinated optimization and control strategy architecture for the EH-DC-MG is shown in Fig. 2.

The BES operates in constant voltage control mode, with the primary objective of serving as a direct voltage support unit for the DC bus. It suppresses power fluctuations in the system through rapid response, thereby maintaining the stability of the bus voltage. Its output power is regulated by a Proportional-Integral (PI) controller, which takes the deviation between the DC bus voltage reference value U_{DC} and the measured voltage U^{BAT} as the input and dynamically adjusts the charging/discharging power of the BES to maintain a constant voltage. The output power of the FC is controlled via a current loop. First, the reference current I_{ref}^{FC} is calculated based on the power command value P_{ref}^{FC} issued by the optimization scheduling layer and the FC terminal voltage U^{FC}. Then, the deviation between I_{ref}^{FC} and the actual current I^{FC} is fed into a PI controller, which generates a PWM duty cycle signal to drive the power converter, thereby achieving precise regulation of the FC output power. The control strategy for the Electrolyzer (EZ) is similar to that of the FC, also adopting a current control method. This enables the EZ to accurately absorb the corresponding power from the DC bus according to the power command value P_{ref}^{EZ} provided by the optimization scheduling layer, achieving accurate tracking of the electric-hydrogen conversion power.

3.2 Optimization Scheduling Layer

3.2.1 Objective Function

The optimization scheduling model aims to minimize the total integrated cost, which accounts for equipment operation and maintenance costs, penalties for wind and PV power curtailment, penalties for power shortage and hydrogen production reduction, as well as battery degradation costs. The objective function is expressed as Eq. (34).

$$\min C = C_{om} + C_{waste} + C_{short} + C_{cut} + C_{cd} \tag{34}$$

where C represents the total system cost, which is the sum of equipment operation and maintenance cost C_{om}, WT/PV curtailment penalty cost C_{waste}, power shortage penalty cost C_{short}, hydrogen production curtailment penalty cost C_{cut}, and battery capacity degradation cost C_{cd}.

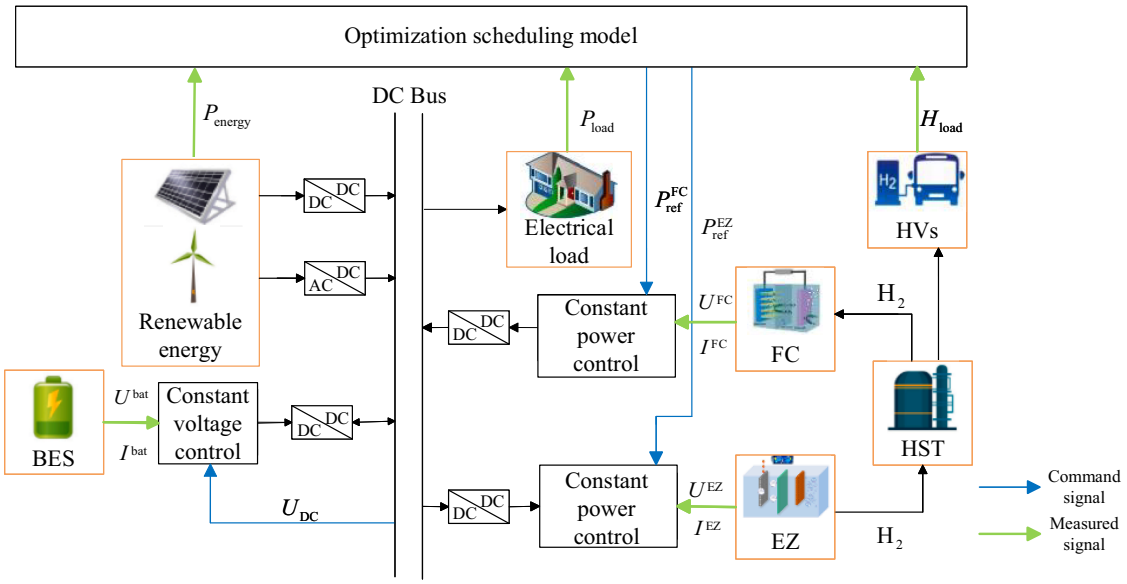

Figure 2: Control diagram of EH-DC-MG

Equipment operation and maintenance cost C_{om} refers to all costs incurred during the operation and usage of equipment. In optimization problems, for estimation purposes, this cost is often calculated by multiplying each equipment's investment cost by an operation and maintenance coefficient. The calculation formulas for C_{om} is shown in Eq. (35).

$$C_{om} = c_{om}^{EL} c^{EL} P_{ra}^{EL} + c_{om}^{FC} c^{FC} P_{ra}^{FC} + c_{om}^{HST} c^{HST} E_{ra}^{HST} + c_{om}^{BESS} c^{BESS} E_{ra}^{BESS} \tag{35}$$

where c_{om}^{EL}, c_{om}^{FC}, c_{om}^{HST}, and c_{om}^{BESS} represent the operation and maintenance coefficients for the EL, FC, HST and BESS, respectively; while c^{EL}, c^{FC}, c^{HST} and c^{BESS} denote the unit investment costs for the EL, FC, HST and BESS, respectively.

C_{waste} refers to the economic penalty incurred when renewable energy output is intentionally reduced or abandoned due to technical or economic constraints, which directly reflects the system's curtailment level of wind and solar power. C_{short} and C_{cut} refer to the economic penalties resulting from implementing penalty measures when insufficient power supply causes electricity deficits, and when insufficient hydrogen supply forces hydrogen load curtailments, respectively. C_{cd} reflects the cost incurred by battery lifespan reduction

per usage cycle. The calculation formulas for C_{waste}, C_{short}, C_{cut}, and C_{cd} are shown in Eqs. (36)–(39), respectively.

$$C_{\text{waste}} = c_{\text{waste}} \times \sum_{t=1}^{T} P_t^{\text{waste}} \tag{36}$$

$$C_{\text{short}} = c_{\text{short}} \times \sum_{t=1}^{T} P_t^{\text{short}} \tag{37}$$

$$C_{\text{cut}} = c_{\text{cut}} \times \sum_{t=1}^{T} H_t^{\text{cut}} \tag{38}$$

$$C_{\text{cd}} = c_{\text{cd}} \times \sum_{t=1}^{T} \left(P_t^{\text{ch}} + P_t^{\text{dis}}\right) \tag{39}$$

where C_{waste}, C_{short}, C_{cut}, and C_{cd} represent the unit cost of renewable energy curtailment, unit power shortage penalty cost, unit hydrogen load curtailment penalty cost, and battery degradation cost per kWh of charge-discharge cycle, respectively; P_t^{waste}, P_t^{short}, H_t^{cut}, P_t^{ch}, and P_t^{dis} represent curtailed renewable energy power, power shortage magnitude, hydrogen load curtailment volume, BES charging power, and BES discharging power, respectively.

3.2.2 Constraints

To ensure real-time matching of electricity-hydrogen production, storage, and consumption while maintaining system stability, the global power balance constraint and hydrogen energy balance constraint are defined in Eqs. (40) and (41), respectively.

$$P_t^{\text{energy}} + P_t^{\text{FC}} + P_t^{\text{dis}} + P_t^{\text{short}} = P_t^{\text{load}} + P_t^{\text{EZ}} + P_t^{\text{ch}} + P_t^{\text{CP}} + P_t^{\text{waste}} \tag{40}$$

$$m_t^{\text{dis}} + m_t^{\text{EZ}} + H_t^{\text{cut}} = m_t^{\text{ch}} + m_t^{\text{FC}} + H_t^{\text{load}} \tag{41}$$

where P_t^{short} denotes the power shortage magnitude; P_t^{load} represents the system electric load power.

To maximize utilization of wind and photovoltaic power resources, curtailed wind and solar generation must satisfy the condition specified in Eq. (42).

$$P_{\text{waste}} \leq \delta_{\text{W}} P_{\text{energy}} \tag{42}$$

where δ_{w}, in the range of [0, 1], denotes the curtailment coefficient of wind and solar generation.

To meet the energy supply reliability requirements of the EH-DC-MG, the power shortage magnitude and hydrogen load curtailment volume must satisfy Eqs. (43) and (44), respectively.

$$P_t^{\text{short}} \leq \delta_{\text{e}} P_t^{\text{load}} \tag{43}$$

$$H_t^{\text{cut}} \leq \delta_{\text{H}} H_t^{\text{load}} \tag{44}$$

where δ_{e} and δ_{H}, in the range of [0, 1], represent the reliability coefficient of electricity and hydrogen supply, respectively.

During periods of abundant WT/PV generation, power injection from distributed energy resources to the bus must be reduced. FC operation shall be prohibited, and BES shall operate in standby or charging mode. During WT/PV generation shortfalls, Electricity-to-hydrogen conversion must be avoided, power supply adequacy shall be prioritized. EZs must be deactivated, and BES shall discharge to mitigate power

deficits within operational limits. Their input/output operating power cannot exceed their rated power and these two devices cannot stand in the operation state simultaneously, as Eqs. (45)–(47).

$$0 \le P_t^{\mathrm{EZ}} \le P_{\mathrm{ra}}^{\mathrm{EZ}} B_t^{\mathrm{EZ}} \tag{45}$$

$$0 \le P_t^{\mathrm{FC}} \le P_{\mathrm{ra}}^{\mathrm{FC}} B_t^{\mathrm{FC}} \tag{46}$$

$$0 \le B_t^{\mathrm{EZ}} + B_t^{\mathrm{FC}} \le 1 \tag{47}$$

where B_t^{EZ} and B_t^{FC} are binary variables to represent the working status of EZ stack and FC at time t, respectively. Specifically, 0 indicates that the device is in the shutdown state and 1 indicates that the device is in the operation state.

3.2.3 Solution Methodology

MILP is capable of simultaneously handling discrete decision variables and continuous variables, such as the on/off status (0–1 integer variables) of equipment and the continuous regulation of power, thereby enabling the precise description of the complex logic involved in the coordinated operation of electric and hydrogen energy storage systems. MILP can guarantee a globally optimal solution or a definitive optimality bound under convex optimization premises; by leveraging efficient algorithms like the branch-and-bound method within mature solvers such as CPLEX, reliable scheduling schemes can be obtained within a reasonable timeframe. Furthermore, its linear structure and standardized modeling framework facilitate the seamless integration of various complex operational constraints (such as the mutual exclusivity of charging and discharging states for energy storage, and tank inventory limits for hydrogen) and offer excellent extensibility. The simulation platform is MATLAB R2018b, programmed with the YALMIP toolbox and solved using the CPLEX solver, on hardware consisting of an Intel(R) Core(TM) i7-11800H CPU @2.30 GHz, 16 GB RAM.

4 Case Analysis and Discussion

4.1 Parameter Description

The detailed technical specifications of electricity-hydrogen conversion and storage devices belonging to EH-DC-MG are summarized in Table 1. The heating value of hydrogen H = 33 kWh/kg [26]. For reliable energy supply and full utilization of new energy sources, the rates of electricity shortage δ_{e}, hydrogen load reduction δ_{H}, wind and solar curtailment δ_{w} are all set as 10% [27]. And the unit penalty costs for curtailed energy C_{waste}, power shortage C_{short}, hydrogen curtailment C_{cut}, and the degradation cost per kWh of charge-discharge cycle for the BES C_{cd} are 0.36 ¥/kWh, 1.2 ¥/kWh, 200 ¥/kg and 0.06 ¥/kWh, respectively [28]. Based on common voltage levels for 150 kW-class DC microgrids, the DC bus nominal voltage U_{DC} is configured at 750 V.

The wind/solar power output and electricity-hydrogen load demand data used in this study are derived from the actual operational data of the Jihong Station in Ulanqab City, Inner Mongolia, and are pre-processed typical scenario data (comprising 23 typical days in total). The use of typical scenario data effectively reduces the complexity of the optimization problem while capturing the system's characteristic operational patterns. These typical scenarios accurately represent the wind and solar power generation characteristics and load fluctuation patterns across different seasons throughout the year in the region. Achieving coordinated operation of equipment under these 23 typical scenarios provides valuable references for conducting coordinated optimization over full-year or longer durations.

The status of renewable generation output and net load demand are shown in Fig. 3. And from left to right, the diagrams in Fig. 4 show the supply-demand matching scenarios on the 1st, 7th, and 23rd typical days. The net load refers to the sum of the hydrogen load converted into an equivalent electrical load and the electrical load.

Table 1: Technical specifications of electricity-hydrogen devices in EH-DC-MG

Device	Technical specifications
HST	V_{ra}^{HST} = 400 L, U_{ra}^{HST} = 200 MPa, $\eta^{HST,ch} = \eta^{HST,dis}$ = 100%, a^{CP} = 0.0015 kWh/mol, SOE_0 = 0.8[1], SOE_{max} = 0.9, SOE_{min} = 0.1, c_{om}^{HST} = 0.04, c^{HST} = 8000 ¥/kg
BES	E_{ra}^{BES} = 140 kWh, P_{ra}^{BES} = 70 kW, $\eta^{BES,ch} = \eta^{BES,dis}$ = 90%, τ = 3% SOC_0 = 0.5[2], SOC_{max} = 0.8, SOC_{min} = 0.2, c_{om}^{BES} = 0.04, c^{BES} = 1200 ¥/kg
FC	x = 99.95%, y = 21%, T_{FC} = 338.15 K, P_{fuel} = 1.5 bar, P_{air} = 1 bar, n^{FC} = 216, E_{ner} = 1.128 V, U_H = 99.59%, η_{low}^{FC} = 48%, η_{mid1}^{FC} = 57%, η_{mid2}^{FC} = 55%, η_{high}^{FC} = 52%, U_o = 59.12%, P_{ra}^{FC} = 19.928 kW, c_{om}^{FC} = 0.04, c^{FC} = 4000 ¥/kW
EZ	U_r^0 = 1.23 V, S = 0.1 m^2, $k_r = 1.93 \times 10^{-3}$ V/K, k^{EZ} = 0.185 V, $k_{f1} = 2.5 \times 10^4$ A^2/m^4, k_{f2} = 96%, $k_1 = 2.54 \times 10^{-2}$ m^2/A, $k_2 = -0.158$ m^2·K/A, $k_3 = 1.212 \times 10^3$ m^2·K^2/A, n^{EZ} = 70, η^{EZ} = 30%, $r_1 = 8.232 \times 10^{-5}$, $r_2 = -4.51 \times 10^{-7}$, P_{ra}^{EZ} = 40 kW, c_{om}^{EZ} = 0.04, c^{EZ} = 2000 ¥/kW

Note: [1]SOE_0 is the initial state of charge for the HST; [2]SOC_0 is the state of charge for the BES.

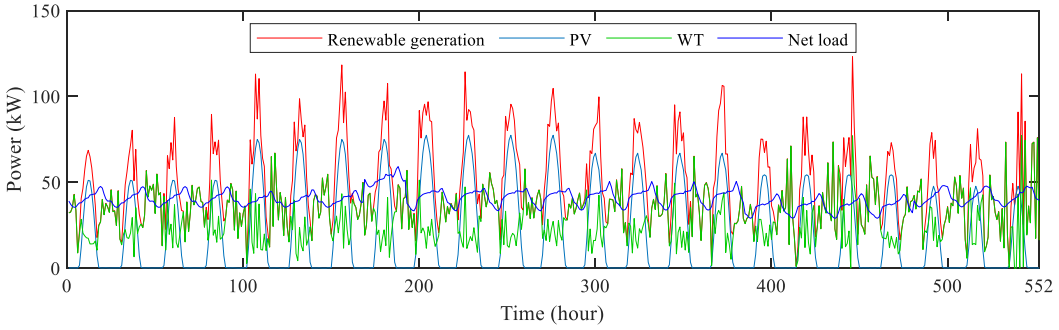

Figure 3: The status of renewable generation and net load

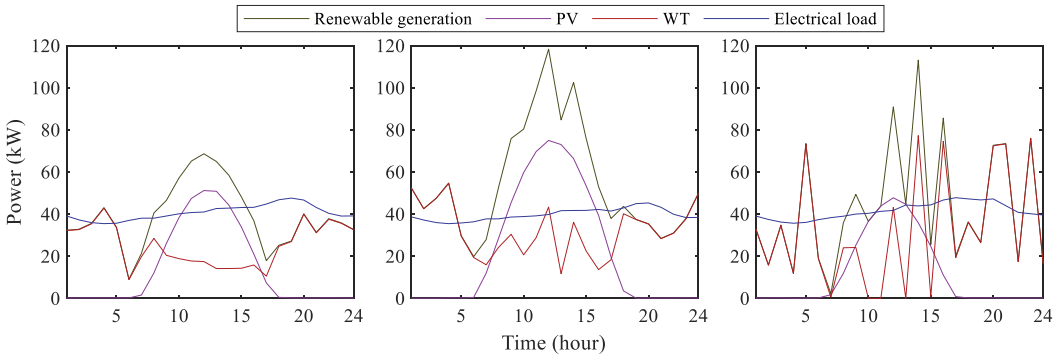

Figure 4: Source-load matching on the typical days 1, 7 and 23

As shown in Figs. 3 and 4, during a typical daily cycle, wind and solar power outputs exhibit distinct patterns. From 00:00 to 06:00, only WTs supply electricity. Although the load demand is low during this period, renewable energy output may still fall short of meeting the demand. Between 10:00 and 15:00, if solar radiation intensity is high, PV output surges significantly. During this time, whether renewable energy output meets load demand primarily depends on solar power, and there will be periods when renewable energy output far exceeds load demand, as illustrated in the middle diagram of Fig. 4. If solar energy is insufficient, the duration during which renewable energy output exceeds load demand will be shorter, as shown in the left diagram of Fig. 4. After 15:00, as both solar and wind resources gradually diminish, renewable energy output declines, while electricity consumption rises to its daily peak. Although WT output increases after 18:00, it may still be insufficient to meet demand. In cases where wind power output significantly exceeds PV output, as depicted in the right diagram of Fig. 4, the high volatility of wind resources leads to a greater mismatch between renewable energy output and load demand. In summary, a significant mismatch exists between renewable energy output and load demand.

4.2 Comparative Analysis of Optimization Results

The status of electrical energy balance and hydrogen energy balance after optimized scheduling are shown in Figs. 5 and 6. When renewable generation exceeds electricity demand, the surplus power is absorbed by both the EZ and BES. One portion is converted into hydrogen by the EZ operation, while the other portion charges the BES. The hydrogen produced by the EZ directly supplies the hydrogen load, with any excess injected into HST for later release upon demand. When renewable generation falls below load requirements, additional electricity must be sourced from the microgrid. This supplemental power is jointly provided by the BES and FC. Under such conditions, the HST must simultaneously supply both the FC and hydrogen load, resulting in significantly higher hydrogen discharge flow rates.

During surplus renewable generation absorption, the EZ takes precedence over BES charging for two primary reasons. Firstly, substantial hydrogen production via EZ is required to meet hydrogen load demands; Secondly, BES exhibits self-discharge phenomena making them unsuitable for long-term storage, while frequent charging cycles accelerate degradation, incurring operational costs—thus avoiding excessive battery charging is imperative.

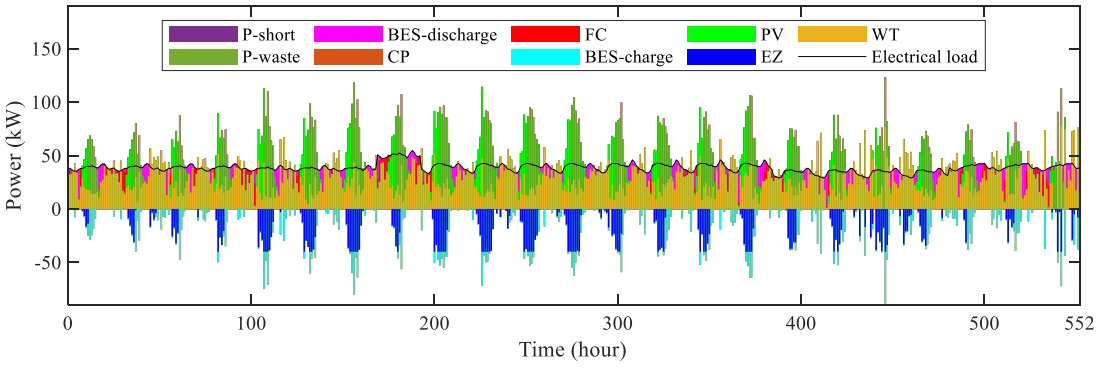

Figure 5: The status of electrical energy balance

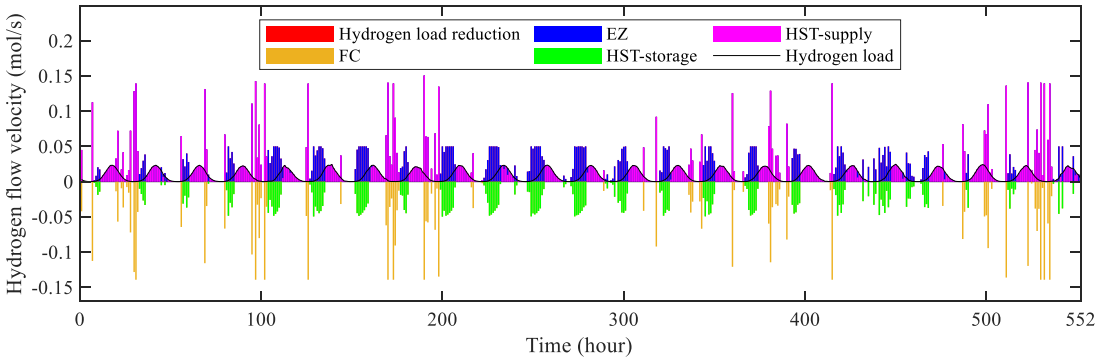

Figure 6: The status of hydrogen energy balance

The variation in energy storage is shown in Fig. 7. When BES reaches its maximum capacity and the EZ operates at rate power, but there is still excess WT and PV output that cannot be utilized, power curtailment occurs. When the BES is depleted to its minimum level and the FC operates at its maximum generation capacity, but the load demand still cannot be met, a power shortfall occurs. Hydrogen load shedding did not occur at any point because the penalty cost for shedding hydrogen load is significantly higher than the cost of a power shortfall.

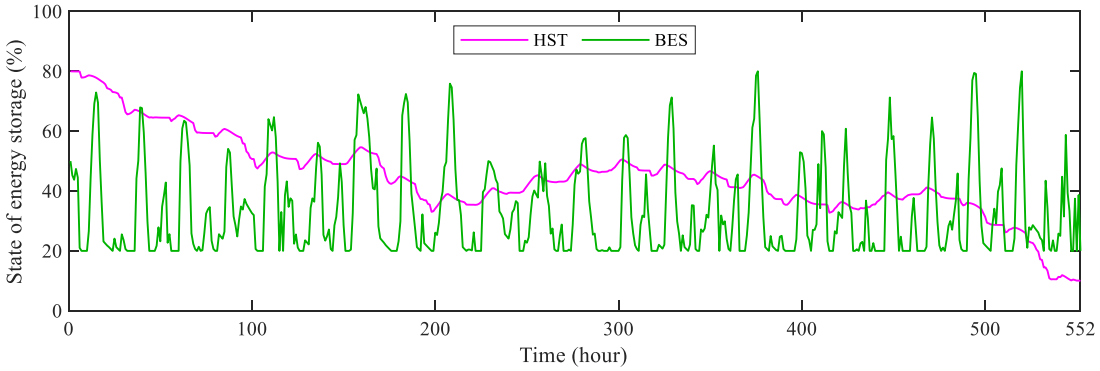

Figure 7: The variation in energy storage status

Multiple runs of the 23 typical scenarios show that the solving time for the optimization scheduling of 23 typical days ranges between 12 and 15 s, which is relatively fast and can meet the computational speed requirements for optimization scheduling.

During this process, the coordinated operation mechanism of the electricity-hydrogen hybrid energy storage system plays a critical role. To systematically validate the effectiveness of the proposed electricity-hydrogen hybrid energy storage architecture in enhancing renewable energy integration capability and power supply quality, a comparative analysis is conducted with a system configuration employing hydrogen storage alone. Scheme 1 corresponds to the proposed electricity-hydrogen hybrid energy storage system, while scheme 2 represents the configuration without the battery energy storage system and the fuel cell. Both schemes undergo optimized scheduling based on the same 23 typical scenarios, and the comparative results of the evaluation indicators are presented in Table 2.

Table 2: Optimization results of schemes 1 and 2

Scheme	Scheme 1	Scheme 2
Total cost (¥)	1909.413	3026.522
Operation and maintenance cost (¥)	1633.315	1209.863
Degradation of BES (¥)	276.098	0
Wind and solar curtailment cost (¥)	0	251.898
Power shortage cost (¥)	0	1564.761
Hydrogen curtailment cost (¥)	0	0
Renewable energy utilization rate (%)	100	97.357
Power shortage rate (%)	0	6.108
Hydrogen curtailment rate (%)	0	0

A comparative analysis reveals that the total system cost of scheme 1 (electricity-hydrogen hybrid energy storage) is approximately 44% lower than that of scheme 2. Although the inclusion of BES in Scheme 1 leads to an increase in operational and maintenance costs by about 35% compared to scheme 2, along with an additional BES lifespan degradation cost, scheme 1 achieves a 2.63% higher renewable energy utilization rate and a zero power shortage rate. As a result, scheme 1 completely avoids penalties associated with wind/solar curtailment and power shortages, thereby significantly reducing the total system cost. The results demonstrate that the proposed coordinated scheduling strategy for the electricity-hydrogen hybrid energy storage system can effectively enhance the level of renewable energy utilization and power supply reliability, while substantially improving the economic performance of system operation.

The typical scenarios can cover most common situations of new energy output and load demand throughout the year, reflecting seasonal variations. However, under abnormal weather conditions, more extreme situations may arise. To validate the system's capability in handling extreme scenarios, two extreme scenarios are specially configured. And the source-load matching under the extreme scenarios is shown in Fig. 8.

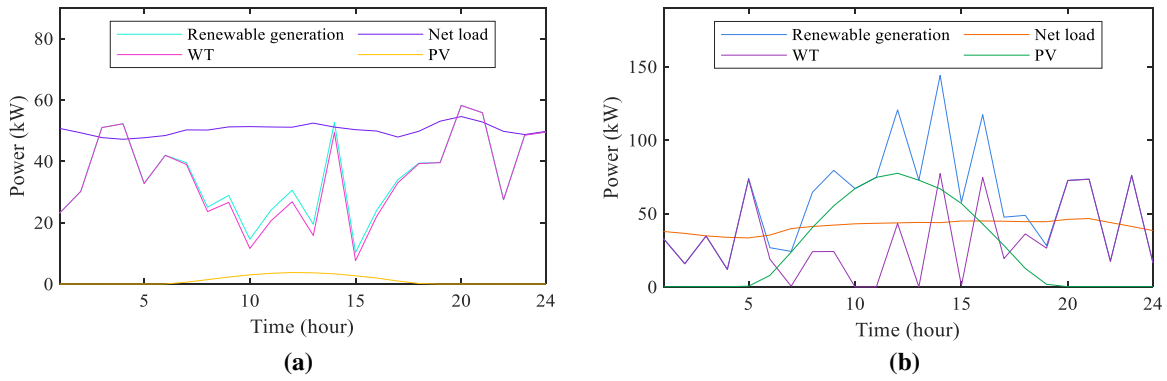

Figure 8: Source-load matching under extreme scenarios

In extreme scenario (a), renewable energy generation is far below load demand. This may occur during heavy rainstorms, where PV output drops to less than 10% of normal levels. Although PV output is not zero, it is extremely low and negligible compared to WT output. Almost all renewable energy output comes from WT, yet it remains below load demand for most of the day. The source-load matching for this scenario is illustrated in Fig. 8a; In extreme scenario (b), renewable energy output significantly exceeds load demand. For instance, during clear weather with strong gusts, both PV and WT output remain high, each substantially contributing to the total renewable energy generation. The renewable energy output surpasses load demand for most of the day while exhibiting extreme volatility. The source-load matching for extreme scenario (b) is illustrated in Fig. 8b.

The status of electrical energy balance and hydrogen energy balance under extreme scenario (a) after optimized dispatch is shown in Figs. 9 and 10. And the variation in energy storage status for HST and BES under extreme scenario (a) is illustrated in Fig. 11.

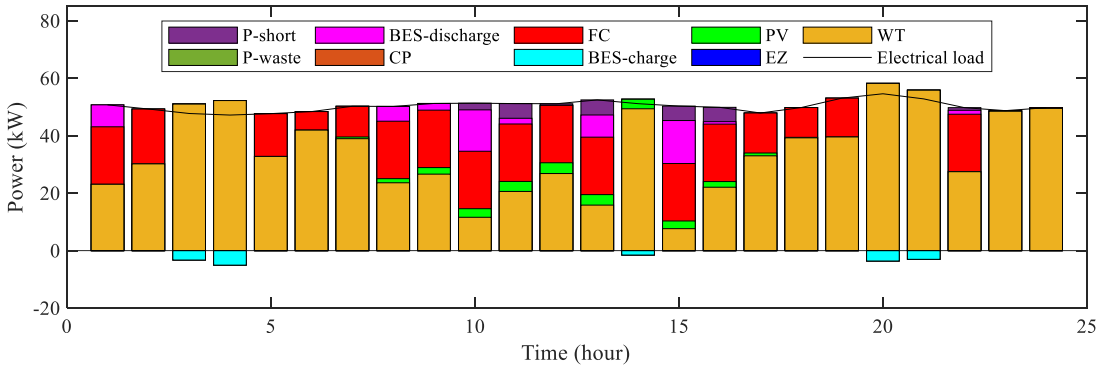

Figure 9: The status of electrical energy balance under extreme scenario (a)

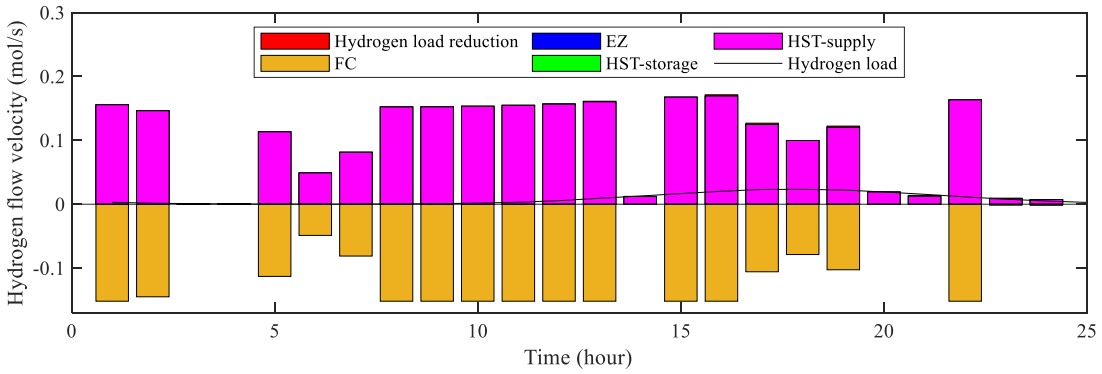

Figure 10: The status of hydrogen energy balance under extreme scenario (a)

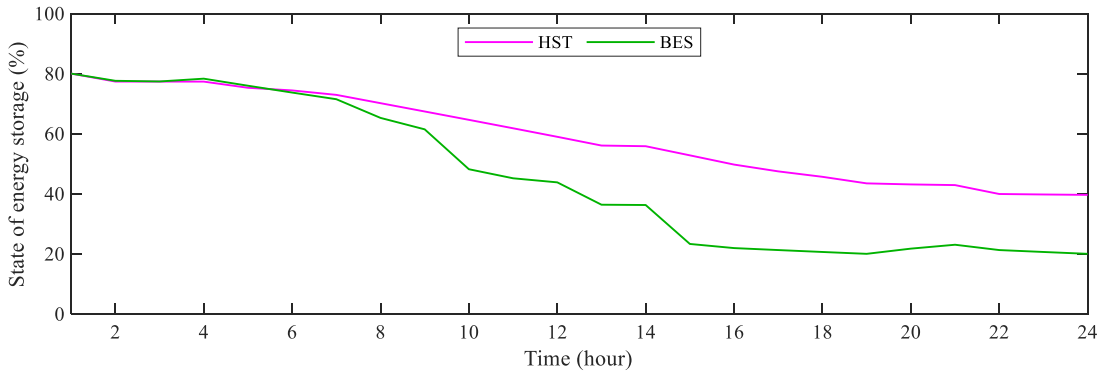

Figure 11: The variation in energy storage status under extreme scenario (a)

In Figs. 9–11, it can be observed that to address this extreme scenario, the initial storage levels of both HST and BES are set high. To mitigate lifetime degradation caused by frequent charging and discharging of BES, the FC is prioritized to meet load demand when renewable energy output is insufficient. Due to ample hydrogen reserves, the FC can operate at maximum power whenever necessary, specifically during hours 1, 8–13, 15–16, and 22. Since renewable energy output is significantly lower than load demand, the EZ is disabled to reduce power consumption. All hydrogen for FC operation and hydrogen load demands are supplied by the HST. During hours 1, 8–11, 13, and 15–16, the FC operates at full capacity but still cannot fully meet demand, prompting the BES to discharge. The optimization scheduling model balances the penalty cost of power shortage and the BES lifetime degradation cost, subject to SOC constraints. Consequently, load shedding is implemented during hours 12–13, 15–16, and 22. As the overall energy supply during the optimization period falls short of demand, any excess energy generated when renewable generation exceed load demand is fully stored in the BES for rapid deployment when needed. This highlights the role of BES in short-term energy storage and power fluctuation mitigation. As shown in Fig. 10, under extreme scenario (a), the optimization scheduling model maintains both SOE and SOC within normal ranges.

The status of electrical energy balance and hydrogen energy balance under extreme scenario (b) after optimized dispatch is shown in Figs. 12 and 13. And the variation in energy storage status for HST and BES under extreme scenario (b) is illustrated in Fig. 14.

In Figs. 12–14, it can be observed that to address this extreme scenario, the initial storage levels of both HST and BES are set low. To mitigate lifetime degradation caused by frequent charging and discharging of BES, excess renewable energy output is prioritized for conversion into hydrogen by the EZ. During hours 12, 14, and 16, the EZ operates at its rated power but still cannot fully absorb the surplus renewable energy, prompting the BES to charge. Although the FC takes precedence over BES in compensating for renewable energy shortfalls, observations indicate that during hours 7 and 22, the BES begins discharging before the FC reaches maximum power. This occurs due to SOC constraints, requiring the BES to discharge appropriately to prevent exceeding the upper SOC limit. The conversion of electricity to hydrogen and its subsequent storage in the HST plays a crucial role in absorbing excess renewable energy when supply significantly exceeds demand. The HST capacity exhibits minimal fluctuation, primarily because the low energy conversion efficiency of EZ consumes substantial electricity for electrolysis while yielding limited hydrogen output. Additionally, the BES experiences a gradual SOC decline even when idle, reflecting its inherent self-discharge losses. This underscores HST's advantage over BES in scenarios requiring long-term, large-scale energy storage due to its superior energy retention capabilities.

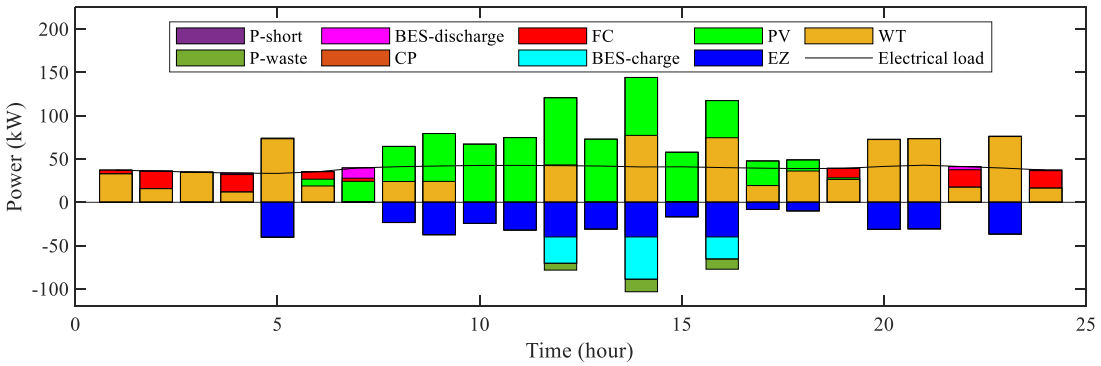

Figure 12: The status of electrical energy balance under extreme scenario (b)

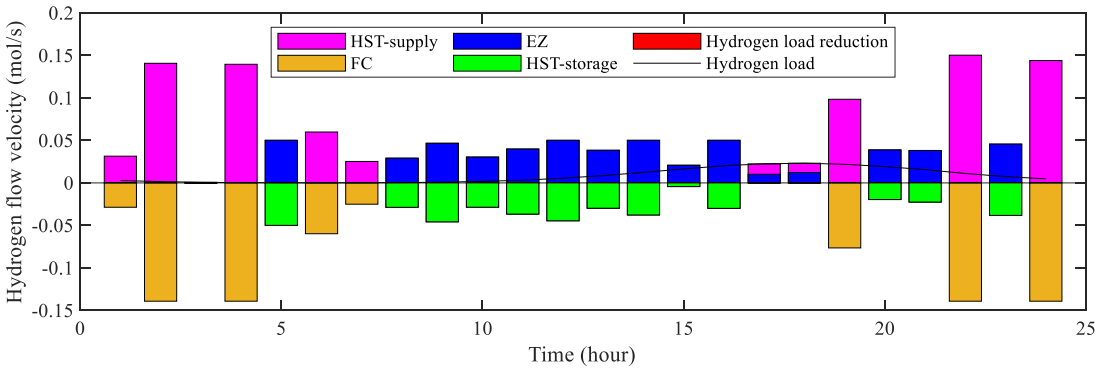

Figure 13: The status of hydrogen energy balance under extreme scenario (b)

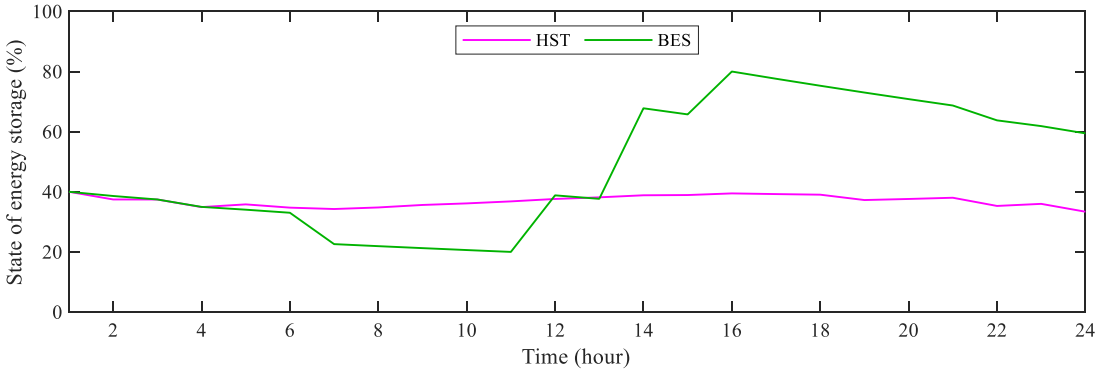

Figure 14: The variation in energy storage status under extreme scenario (b)

The cost items and evaluation metrics of the optimized system under extreme scenarios are presented in Table 3.

As shown in Table 3, under extreme extreme scenario (a), system achieves a 100% renewable energy utilization rate, with a power shortage rate of only 2.003% and a hydrogen load curtailment rate of 5.081%, which are significantly below the 10% upper limit for power quality constraints. Under extreme extreme scenario (b), the renewable energy utilization rate reached 97.572%, with no power shortage or hydrogen curtailment. In summary, the optimization results demonstrate that even under extreme scenarios, the

scheduling model effectively coordinates power allocation among devices, achieving high utilization of renewable energy while ensuring energy supply quality.

Table 3: Cost items and evaluation metrics of the optimized system under extreme scenarios

Extreme scenario	Extreme scenario (a)	Extreme scenario (b)
Degradation of BES (¥)	4.38	7.35
Wind and solar curtailment cost (¥)	0	12.23
Power shortage cost (¥)	29.00	0
Hydrogen curtailment cost (¥)	14.33	0
Renewable energy utilization rate (%)	100	97.572
Power shortage rate (%)	2.003	0
Hydrogen curtailment rate (%)	5.081	0

4.3 Simulation Results Analysis

Use the optimization results of the typical day 1 as a reference command to conduct a system operation simulation, thereby verifying the tracking effectiveness of the employed control method for the command. The electrical power tracking performance are illustrated in Figs. 15 and 16.

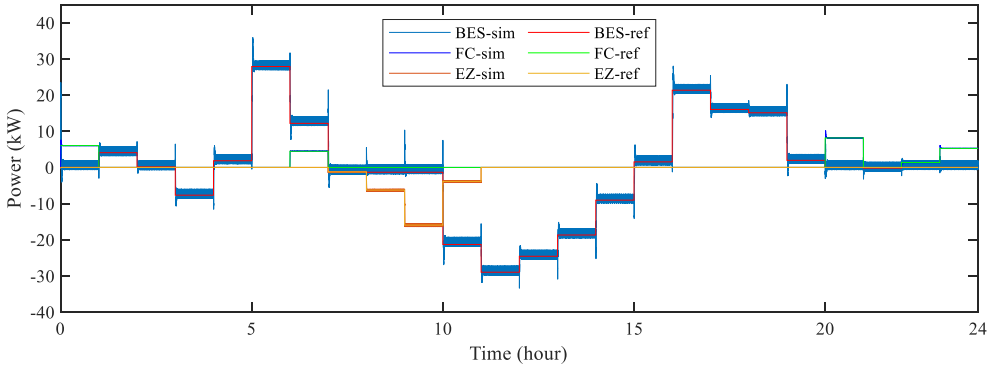

Figure 15: Electrical power tracking performance

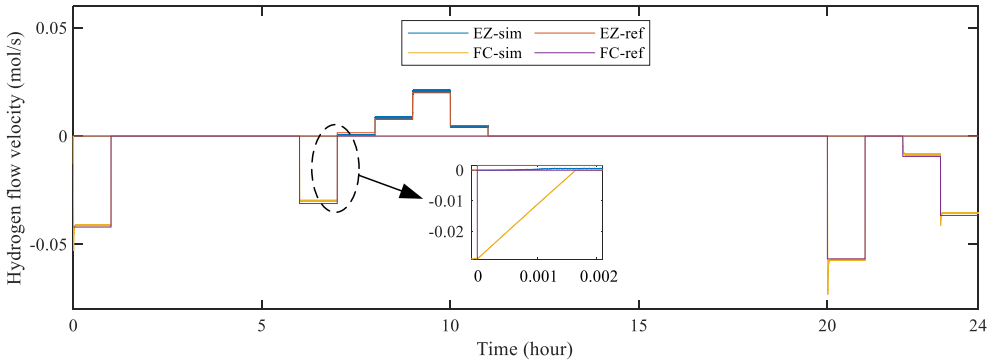

Figure 16: Hydrogen flow velocity simulation results

In the legends of Figs. 15 and 16, '-sim' denotes the simulated values, while '-ref' denotes the reference values. And as shown in Fig. 15, both the EZ and FC effectively track the power reference commands in the Simulink-based simulation experiment, and the response time is less than 2 ms. Although the BES operates under constant voltage control, its power output still follows the reference values. This occurs because the BES undertakes the task of maintaining system voltage stability and power balance, and its power output following the dispatch reference values demonstrates that the simulation system has achieved correct power balancing. It can be observed that the BES exhibits significant overshoot during power regulation and noticeable ripple in steady-state conditions. These issues arise from the complex nonlinear characteristics of the BES and the switching actions of DC converter components. More advanced converter control strategies, such as virtual synchronous machine control, can be employed to improve its transient performance, while filters can be added to reduce ripple. This paper will not delve into an in-depth investigation of these aspects.

Fig. 17 shows the hydrogen flow rate errors resulting from the linear approximation of the electro-hydrogen conversion efficiency for the EZ and FC. Calculations indicate that the steady-state average error of the hydrogen flow rates for both the EZ and the FC over a day is approximately 1.97%, which is below the 3% control accuracy requirement. Furthermore, the core decisions of the optimal dispatch, namely, when to start and stop the EZ and FC, and the power distribution between the battery and hydrogen storage under different scenarios, are driven primarily by the system's energy balance and cost structure such as penalty costs. Therefore, the errors introduced by the model linearization are considered acceptable for engineering purposes.

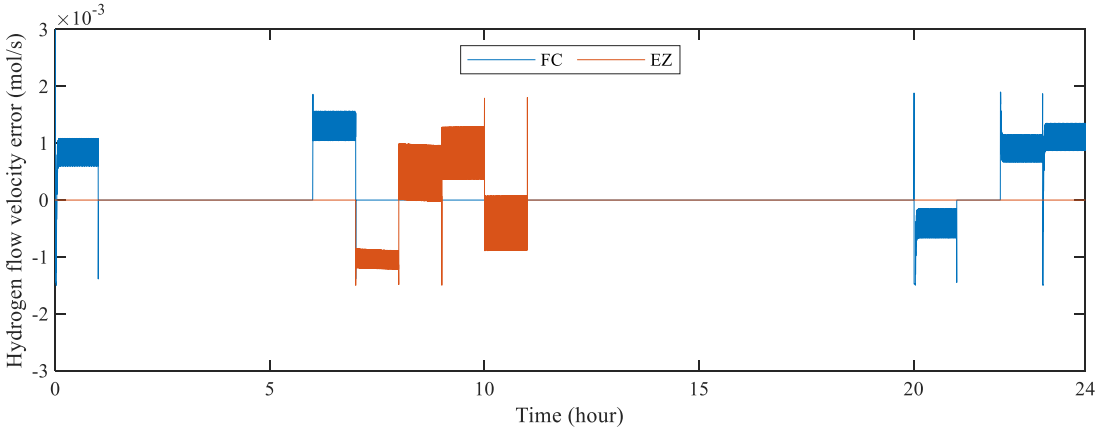

Figure 17: Hydrogen flow velocity error

The fluctuation of the DC bus voltage is shown in Fig. 18. It can be observed that power adjustment by the device leads to fluctuations in the DC bus voltage. Particularly, when the BES performs power adjustments with a large magnitude, it causes significant fluctuations in the DC bus voltage. Moreover, when the BES power is increased, the DC bus voltage decreases; when the BES power is decreased, the DC bus voltage rises. Typically, at the 5th and 10th hours, the substantial increase and decrease in BES power resulted in a drop and rise in the DC bus voltage, respectively. The maximum absolute fluctuation of the DC bus voltage occurred at the 5th hour, measuring only 2.8074 V, which represents a fluctuation amplitude of 0.37%. This is significantly lower than the 5% safety operation requirement. Therefore, it is concluded that the control strategy adopted in this study effectively maintains the stability of the DC bus voltage and ensures the safe operation of the system.

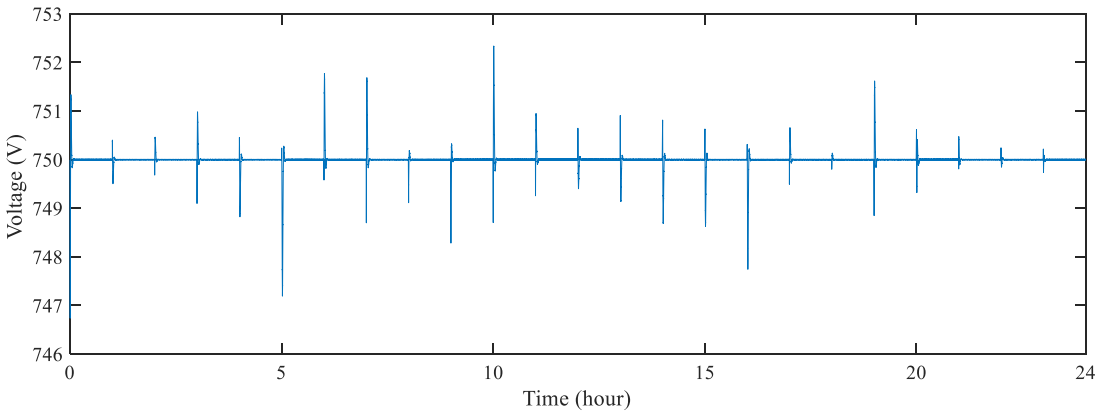

Figure 18: DC bus voltage

5 Conclusion

In this paper, a hierarchical coordinated optimization control strategy for EH-DC-MG is proposed, aiming to support its economic operation, renewable energy utilization and reliable energy supply. The main findings are summarized as follows: 1) The collaborative operation of long-term hydrogen energy storage and short-term battery energy storage effectively mitigates source-load imbalances. Under the proposed strategy, the SOE of the HST is maintained between 10% and 90%, while the SOC of the BES is regulated within 20%–80%, ensuring both operational safety and long-term cycling capability. This complementary mechanism significantly improves the flexibility and reliability of the EH-DC-MG; 2) The hybrid electricity-hydrogen energy storage system effectively overcomes the limitations of single-form energy storage in terms of duration and power response through the synergistic complementarity of long-term hydrogen storage and short-term battery storage. This provides critical support for achieving higher renewable energy utilization rates and enhanced energy supply reliability. The optimal scheduling model based on MILP enables the EH-DC-MG to significantly improve renewable energy utilization while ensuring power supply quality. Under extreme operating scenarios, the proposed strategy demonstrates remarkable adaptability: in conditions of severe renewable energy shortage, the system's power shortage rate is only 2.003%, well below the 10% threshold requirement. Conversely, in scenarios with excessive renewable energy generation, the system still achieves a high utilization rate of 97.572%. These results fully illustrate the comprehensive advantages of the electricity-hydrogen hybrid system in multi-timescale energy balance and operational resilience. 3) The adopted control strategy can maintain the stability of the DC bus voltage, with the maximum voltage fluctuation being less than 0.3%, which is far below the 5% safe operation requirement. In summary, the hierarchical coordinated optimization control strategy proposed in this study provides a comprehensive solution for the efficient, stable, and economical operation of EH-DC-MGs, offering both theoretical and practical value for future renewable-dominated microgrid systems.

This study still has some limitations, which also point out the direction for future research. Specifically, the model does not directly incorporate an uncertainty model for short-term forecasting errors of wind and solar power, which poses a critical challenge in practical operation. Additionally, reasonable linear approximations were applied to the nonlinear efficiency characteristics of the equipment. While these approximations meet accuracy requirements under most operating conditions, they may introduce deviations at extreme operating points. Future research could focus on integrating uncertainty-aware optimization and refined modeling to better approximate real-world physical conditions, which would be more conducive to increasing the penetration of renewable energy and ensuring supply reliability in engineering practice. Furthermore, improving power electronic converter control strategies to enhance the dynamic performance

of equipment, and extending the system model to multi-bus and AC/DC hybrid distribution network architectures while considering the impact of power flow and voltage constraints, will be important directions for advancing the practical application of electricity-hydrogen hybrid systems.

Acknowledgement: This paper was completed with the hard help of every author.

Funding Statement: This work was supported by the Science and Technology Project of China Southern Power Grid under Grant ZBKJXM20240021.

Author Contributions: Xinhao Lin proposed the concept, method, principle and first draft of the manuscript. Lei Yu, Shuyin Duan and Yinliang Liu were responsible for data analysis, drawing, and formulating the conclusions of this study. Lvzerui Yuan and Xiao Chen contributed through review, modification, and final approval of the manuscript. Yiqing Lian provided supervision and approval of the work. All authors reviewed the results and approved the final version of the manuscript.

Availability of Data and Materials: The authors confirm that the data supporting the findings of this study are available within the article.

Ethics Approval: Not applicable.

Conflicts of Interest: The authors declare no conflicts of interest to report regarding the present study.

References

1. Kostevšek A, Klemeš JJ, Varbanov PS, Čuček L, Petek J. Sustainability assessment of the locally integrated energy sectors for a slovenian municipality. J Cleaner Prod. 2015;88:83–9. doi:10.1016/j.jclepro.2014.04.008.
2. Boukettaya G, Krichen L. A dynamic power management strategy of a grid connected hybrid generation system using wind, photovoltaic and flywheel energy storage system in residential applications. Energy. 2014;71(1):148–59. doi:10.1016/j.energy.2014.04.039.
3. Bukhsh WA, Zhang C, Pinson P. An integrated multiperiod OPF model with demand response and renewable generation uncertainty. IEEE Trans Smart Grid. 2016;7(3):1495–1503. doi:10.1109/TSG.2015.2502723.
4. Li J, Li G, Ma S, Liang Z, Li Y, Zeng W. Modeling and simulation of hydrogen energy storage system for power-to-gas and gas-to-power systems. J Mod Power Syst Clean Energy. 2023;11(3):885–95. doi:10.35833/MPCE.2021.000705.
5. Martínez L, Fernández D, Mantz R. Passivity-based control for an isolated DC microgrid with hydrogen energy storage system. Int J Hydrogen Energy. 2024;67(12):1262–9. doi:10.1016/j.ijhydene.2024.01.324.
6. Tao Y, Qiu J, Lai S, Zhao J. Integrated electricity and hydrogen energy sharing in coupled energy systems. IEEE Trans Smart Grid. 2021;12(2):1149–62. doi:10.1109/TSG.2020.3023716.
7. Garcia-Torres F, Valverde L, Bordons C. Optimal load sharing of hydrogen-based microgrids with hybrid storage using model-predictive control. IEEE Trans Ind Electron. 2016;63(8):4919–28. doi:10.1109/TIE.2016.2547870.
8. Gulzar MM, Iqbal A, Sibtain D, Khalid M. An innovative converterless solar PV control strategy for a grid connected hybrid PV/wind/fuel-cell system coupled with battery energy storage. IEEE Access. 2023;11(4):23245–59. doi:10.1109/ACCESS.2023.3252891.
9. Abdelghany MB, Al-Durra A, Gao F. A coordinated optimal operation of a grid-connected wind-solar microgrid incorporating hybrid energy storage management systems. IEEE Trans Sustain Energy. 2024;15(1):39–51. doi:10.1109/TSTE.2023.3263540.
10. Pei W, Zhang X, Deng W, Tang C, Yao L. Review of operational control strategy for DC microgrids with electric-hydrogen hybrid storage systems. CSEE J Power Energy Syst. 2022;8(2):329–46. doi:10.17775/CSEEJPES.2021.06960.

11. Guerrero JM, Loh PC, Lee T-L, Chandorkar M. Advanced control architectures for intelligent microgrids—part II: power quality, energy storage, and AC/DC microgrids. IEEE Trans Ind Electron. 2013;60(4):1263–70. doi:10.1109/TIE.2012.2196889.
12. Pan G, Gu W, Lu Y, Qiu H, Lu S, Yao S. Optimal planning for electricity-hydrogen integrated energy system considering power to hydrogen and heat and seasonal storage. IEEE Trans Sustain Energy. 2020;11(4):2662–76. doi:10.1109/TSTE.2020.2970078.
13. Tahim APN, Pagano DJ, Lenz E, Stramosk V. Modeling and stability analysis of islanded DC microgrids under droop control. IEEE Trans Power Electron. 2015;30(8):4597–607. doi:10.1109/TPEL.2014.2360171.
14. Li X, Zhang S, Wang C, Li Y, Chen A, Feng Y. Observer-based DC voltage droop and current feed-forward control of a DC microgrid. IEEE Trans Smart Grid. 2018;9(5):5207–16. doi:10.1109/TSG.2017.2684178.
15. Sahoo S, Mishra S. An adaptive event-triggered communication-based distributed secondary control for DC microgrids. IEEE Trans Smart Grid. 2018;9(6):6674–83. doi:10.1109/TSG.2017.2717936.
16. Zhu Z, Liu X, Kong X, Ma L, Lee KY, Xu Y. PV/Hydrogen DC microgrid control using distributed economic model predictive control. Renew Energy. 2024;222(1):1–11. doi:10.1016/j.renene.2023.119871.
17. Karami Z, Shafiee Q, Khayat Y, Yaribeygi M, Dragičević T, Bevrani H. Decentralized model predictive control of DC microgrids with constant power load. IEEE J Emerging Sel Top Power Electron. 2021;9(1):451–60. doi:10.1109/JESTPE.2019.2957231.
18. Ahmad S, Shafiullah M, Ahmed CB, Alowaifeer M. A review of microgrid energy management and control strategies. IEEE Access. 2023;11(1):21729–57. doi:10.1109/ACCESS.2023.3248511.
19. Manbachi M, Ordonez M. Intelligent agent-based energy management system for islanded AC–DC microgrids. IEEE Trans Ind Informat. 2020;16(7):4603–14. doi:10.1109/TII.2019.2945371.
20. Senapati MK, Al Zaabi O, Al Hosani K, Al Jaafari K, Pradhan C, Ranjan Muduli U. Advancing electric vehicle charging ecosystems with intelligent control of DC microgrid stability. IEEE Trans Ind Appl. 2024;60(5):7264–78. doi:10.1109/TIA.2024.3413052.
21. Venayagamoorthy GK, Sharma RK, Gautam PK, Ahmadi A. Dynamic energy management system for a smart microgrid. IEEE Trans Neural Netw Learn Syst. 2016;27(8):1643–56. doi:10.1109/TNNLS.2016.2514358.
22. Du Y, Li F. Intelligent multi-microgrid energy management based on deep neural network and model-free reinforcement learning. IEEE Trans Smart Grid. 2020;11(2):1066–76. doi:10.1109/TSG.2019.2930299.
23. Tremblay O, Dessaint L-A. Experimental validation of a battery dynamic model for EV applications. World Electr Veh J. 2009;3(2):289–98. doi:10.3390/wevj3020289.
24. Jain S, Jiang J, Huang X, Stevandic S. Modeling of fuel-cell-based power supply system for grid interface. IEEE Trans Ind Appl. 2012;48(4):1142–53. doi:10.1109/TIA.2012.2199454.
25. Esmaeilian HR, Fadaeinedjad R. Resolving power quality issues raised by aerodynamic aspects of wind turbine in isolated microgrids using fuel cell/electrolyzer system. IEEE Trans Sustain Energy. 2016;7(3):1274–83. doi:10.1109/TSTE.2016.2544102.
26. Liu N, Zhang K, Zhang K. Coordinated configuration of hybrid energy storage for electricity-hydrogen integrated energy system. J Energy Storage. 2024;95(1):1–14. doi:10.1016/j.est.2024.112590.
27. Lin L, Zheng X, Gu J. Optimal dispatching of combined heat and power system considering the power demand elasticity of hydrogen storage active load. IEEE Trans Ind Appl. 2022;58(2):2760–70. doi:10.1109/TIA.2021.3105618.
28. Leng R, Li Z, Xu Y. Two-stage stochastic programming for coordinated operation of distributed energy resources in unbalanced active distribution networks with diverse correlated uncertainties. J Mod Power Syst Clean Energy. 2023;11(1):120–31. doi:10.35833/MPCE.2022.000510.